Photo-electrochemical characterization of CIGSn lamellar compounds: potential candidates for photoinduced applications

Amal Belhcen, Adèle Renaud, Catherine Guillot-Deudon, Ludovic Arzel, Benoit Corraze, Nicolas Barreau, Stéphane Jobic, Maria Teresa Caldes

Electrochimica Acta 511 (2025) 145391

Contents lists available at ScienceDirect

Electrochimica Acta

journal homepage: www.journals.elsevier.com/electrochimica-acta

Photo-electrochemical characterization of $CIGS_n$ lamellar compounds: potential candidates for photoinduced applications

Amal Belhcen [a], Adèle Renaud [b,*], Catherine Guillot-Deudon [a], Ludovic Arzel [a], Benoit Corraze [a], Nicolas Barreau [a], Stéphane Jobic [a], Maria Teresa Caldes [a,*]

[a] Nantes Université, CNRS, Institut des Matériaux de Nantes Jean Rouxel, IMN, F-44000 Nantes, France
[b] Univ. Rennes, CNRS, ISCR-UMR, 6226, F-35000 Rennes, France

ARTICLE INFO

Keywords:
$CIGS_n$
Flat band potential
Electronic structure
Ambipolarity

ABSTRACT

Metal chalcogenide semiconductors are being widely investigated for applications in solar energy conversion, such as photovoltaics and visible light photocatalysis. Herein, an initial assessment of potentialities of new lamellar chalcogenides named $CIGS_n$ is provided, while comparing them with that of the well-known CIGS chalcopyrite. The main difference between CIGS and $CIGS_n$ compounds concerns their electronic properties and more precisely the nature of charge carriers. $Cu_{0.32}In_{1.74}Ga_{0.84}S_4$ ($CIGS_4$) is an n-type semiconductor, unlike the chalcopyrite $CuIn_{0.7}Ga_{0.3}S_2$ (CIGS) that is a p-type semiconductor. More noticeable, $Cu_{1.44}In_{2.77}Ga_{0.76}S_6$ ($CIGS_6$) and in a lesser extent $Cu_{0.65}In_{1.75}Ga_{1.4}S_5$ ($CIGS_5$), exhibit an ambipolar character with a slight predominance of electron transport. The Fermi levels of all lamellar $CIGS_n$ compounds are similar (-4.5 eV) and higher that of the chalcopyrite CIGS (-5.1 eV). In addition, the charge carrier densities of $CIGS_n$ compounds (10^{14}–10^{17} cm^{-3}) are significantly lower than that of CIGS (10^{20} cm^{-3}), which is consistent with their higher resistivity. Photoluminescence measurements and OCP decays suggest much more in-gap defect states in the lamellar compounds. These results suggest that $CIGS_n$ compounds would not be suitable for photovoltaic applications. Nevertheless, their energy bands show an interesting positioning, with respect to redox potentials involved in water splitting and CO_2 reduction. In addition, ambipolarity could enhance the efficiency of catalytic reactions, because a type of minority charge carriers does not limit the charge transport.

1. Introduction

Metal chalcogenides semiconductors stand out as promising candidates for different light driven applications such as photovoltaics (PV) and photocatalysis [1,2]. Formally, the great interest of such compounds resides in their optical properties with often a gap lower less than 3 eV. That makes them active in the visible range of the solar light, with concomitantly higher propensity than oxides to absorb light due to higher covalency of chemical bonds. Moreover, a lower effective mass of carriers may be expected, due to lesser localization effects and larger dispersion of electronic bands. This should favour the separation of electron-hole pairs, migration of photo-generated charges toward the surface, and consequently chemical reactivity towards species to reduce or to oxidize. Moreover, two-dimensional (2D) metal chalcogenides, especially materials with van der Waals gap prepared as lamellas, offer additional advantages. Formally, the 2D nature reduces the diffusion length of charge carriers, which improves the kinetics of photoinduced reactions on the surface. As well, the band gap energy and band positions of 2D materials usually depend on the overall thickness of the structural slabs, which can be employed to modify their photo-generated properties [3]. Among these materials, copper-based sulphide chalcogenides, especially ternary and quaternary compounds, are very interesting, due to their wide range of composition and their structural flexibility, which allows the adjustment of their optical properties. Accordingly, the pseudo-ternary Cu_2S-In_2S_3-Ga_2S_3 system is currently the focus of exploratory research to identify new compounds for photo-induced applications.

Recently, new quaternary lamellar compounds named $CIGS_n$ have been reported in the literature [4], namely $Cu_{0.32}In_{1.74}Ga_{0.84}S_4$ ($CIGS_4$), $Cu_{0.65}In_{1.75}Ga_{1,4}S_5$ ($CIGS_5$) and $Cu_{1.44}In_{2.77}Ga_{0.76}S_6$ ($CIGS_6$). As shown in Fig. 1, $CIGS_n$ compounds present a 2D structure built upon infinite $^2/_\infty[InS_2]$ layers based on [InS_6] octahedral sharing edges, on which condense, on both sides, mono-, bi-, or tri-$^2/_\infty$[MS] layers (i.e., [MS_4] tetrahedral sharing corners) with M = Cu, In, Ga. The $[M_{(Td)})_{n\text{-}2}(In_{(Oh)}]$

* Corresponding authors.
E-mail addresses: adele.renaud@univ-rennes.fr (A. Renaud), maite.caldes@cnrs-imn.fr (M.T. Caldes).

https://doi.org/10.1016/j.electacta.2024.145391
Received 14 April 2024; Received in revised form 31 October 2024; Accepted 19 November 2024
Available online 22 November 2024

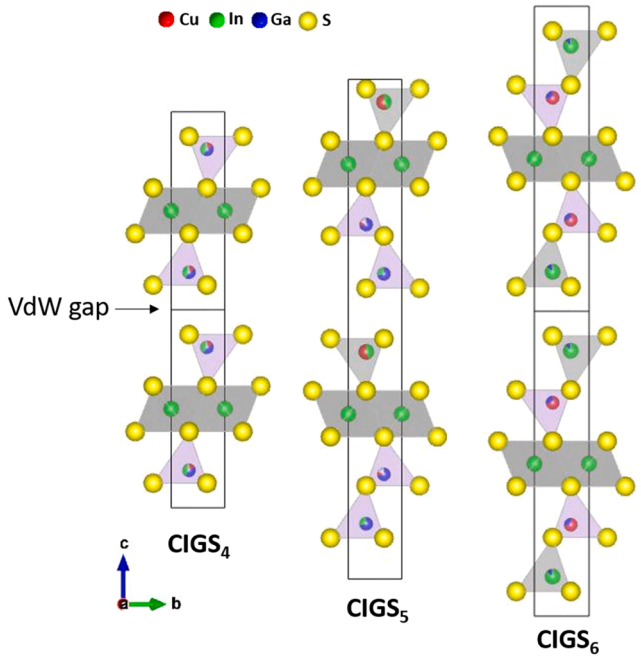

Fig. 1. Schematic representation of $CIGS_n$ crystal structures

S_n slabs, where n is the total number of sulphur layers, are separated from each other by a van der Waals gap. Let us put the emphasis that tetrahedral sites (Td) exhibit intrinsic cationic vacancies and mixed occupancy (Cu^+, In^{3+} and Ga^{3+}), allowing chemical composition tuning.

These lamellar materials are potentially interesting for photoinduced applications for several reasons. First, $CIGS_n$ compounds exhibit optical gaps (1.7 - 1.9 eV) comparable to that of the chalcopyrite $Cu(In_{0.7}Ga_{0.3})S_2$ (CIGS), studied as absorber in tandem solar cells [5], but also as photocatalyst for hydrogen evolution reaction (HER) [6]. Second, $CIGS_n$ phases are isostructural with ZIS_n compounds (i.e., $ZnIn_2S_4$ and $Zn_3In_2S_6$), extensively investigated as visible-photocatalysts for HER [7, 8]. Given the beneficial role that lattice defects could have on photocatalytic properties [9], the existence of native cationic vacancies and mixed-cationic occupancy in $CIGS_n$ compounds could be considered as an advantage over ZIS_n photocatalysts. Third, $CuIn_3Ga_2S_8$, isostructural with $Ag_{1.12}In_{3.7}Ga_{2.68}S_{10}$ that exhibits a $CIGS_5$ type-structure, have been studied for solar hydrogen production, evidencing a significant efficient photocatalystic activity in the visible [10].

Therefore, the aim of this work is to provide an initial assessment of potentialities of $CIGS_n$ compounds for photovoltaic and visible light photo-catalysis applications, while comparing them with that of the well-known CIGS chalcopyrite. This requires the evaluation of a number of intrinsic properties such as visible light absorption, optical band gap, nature of the majority carriers and carrier lifetime. The position of the valence and conduction bands on an absolute scale, as well as that of the Fermi level were also determined. For this purpose, an analytical approach combining diffuse reflectance experiments, electrochemical measurements and X-ray photoelectron spectroscopy (XPS) was implemented.

2. Experimental section

$CIGS_n$ powders with n= 4, 5 and 6 were synthesised by a solid-state reaction route, following the protocol previously reported [4]. $Cu_{0.32}In_{1.74}Ga_{0.84}S_4$ ($CIGS_4$), $Cu_{0.65}In_{1.75}Ga_{1.4}S_5$ ($CIGS_5$), $Cu_{1.44}In_{2.77}Ga_{0.76}S_6$ ($CIGS_6$) lamellar compounds and $CuIn_{0.7}Ga_{0.3}S_2$ (CIGS) chalcopyrite were prepared from binary precursors (i.e., metal sulphides Cu_2S, Ga_2S_3 and In_2S_3) mixed in stoichiometric ratios. The mixture was sealed in a silica tube, heated up to 800°C for 48h and then cooled down to room temperature by quenching. In the case of $CIGS_6$, an additional annealing is required.

For (photo)electrochemical measurements (PEC), CIGS and $CIGS_n$ sintered pellets (~ 0.8 cm^2 of diameter) were prepared by spark plasma sintering (SPS) in order to improve their compactness. Namely, samples were pressed under 38 MPa under argon atmosphere in a graphite die at high temperature (500°C) for 5 min. The working electrodes were prepared by sticking the pellets to a copper wire using a conductive carbon glue, then dipped in the resin and finally polished to obtain a flatten smooth surface.

Chronopotentiometry, current−potential curves and electrochemical impedance spectroscopy, were performed using a three electrodes cell with platinum, $CIGS_n$ pellets and Ag/AgCl as counter, working and reference electrodes, respectively. KCl aqueous solution (0.5 M) was used as electrolyte (pH ≈ 6). PEC measurements were carried out under chopped illumination using an MI-LED illuminator (Edmund Optics). The corresponding emission spectrum and the instrumental setup are shown in supplementary information (Fig. S1).

Impedance spectra were measured under dark in a frequency range from 100 Hz to 100 kHz. Nyquist diagrams of all compounds, depicted in Fig. S2, were plotted from the electrochemical impedance spectroscopy (EIS) measurements in the dark. The equivalent circuit used to fit them consisted to a simplified Randles circuit with neglecting Warburg as shown in insets. The capacitance of the space charge region C_{SC} at the surface of the semiconductor and the interfacial electrical double charge layer, principally controlled by the Helmholtz layer in the electrolyte, contribute to the total capacitance C. Indeed, due to the high concentration of the electrolyte (> 0.1 M), the Gouy-Chapman layer can be neglected. As the capacity of the Helmholtz layer C_H is notably higher than C_{SC}, C^{-2} is approximately equal to C_{SC}^{-2}.

The Mott−Schottky (MS) plots were plotted in a potential range of −0.8 to 0.2 V vs. Ag/AgCl at relatively high frequencies (1−10 kHz) to neglect the diffusion phenomena, according to the formula below:

$$\frac{1}{{C_{SC}}^2} = \frac{2}{\varepsilon\varepsilon_0 e A^2 N}\left(V - V_{fb} - \frac{kT}{e}\right) \quad (1)$$

where Csc is the capacitance of the space-charge region, ε_0 corresponds to the vacuum permittivity, ε is the relative permittivity of the semiconductor, A is the surface of the probed semiconductor in contact with the electrolyte, N is the donor density (formally, electron donor concentration N_D for an n-type semiconductor or hole acceptor concentration N_A for a p-type semiconductor), k is the Boltzmann constant, T is the temperature and e is the electron charge. Since $\frac{kT}{e}$ equals to 0.025 V at 20°C, this term is generally neglected. Consequently, Eq. (1) can be simplified and replaced by Eqs. (2) and (3):

$$\frac{1}{Csc^2} \approx \frac{2}{\varepsilon\varepsilon_0 A N_A}\left(V - V_{fb}\right) \quad (2)$$

$$\frac{1}{Csc^2} \approx \quad -\frac{2}{\varepsilon\varepsilon_0 A N_D}\left(V - V_{fb}\right) \quad (3)$$

Due to the difference in redox potential between the semiconductor (determined by the Fermi level) and the electrolyte, bringing the latter into contact causes the creation of a double layer at the interface. Typically, the semiconductors are in depletion conditions at equilibrium (at open-circuit). Indeed, for an n-type (p-type) semiconductor, the Fermi level is typically higher (lower) than the redox potential of the electrolyte, and hence electrons (holes) are transferred from the electrode into the solution. Therefore, there is a positive (negative) charge associated with the space charge region, and this is reflected in an upward (downward) bending of the band edges. Thus, regarding the sign and the value of the slope obtained by scanning from depletion to accumulation conditions, the type of semiconductor and the donor or acceptor density N_D or N_A can be determined respectively. Their values were approximated by using for calculations, the permittivity of the

chalcopyrite CIGS ($\varepsilon = 13.6$) [11] and the geometric surface of the pellet as contact surface semiconductor/electrolyte (porosity of the pellet was not taken at all into account). Consequently, N_A and N_D calculated values have to be regarded with precaution, and only as overall indicators (estimation of the order of magnitude). The flat band potentials V_{fb} were determined versus Ag/AgCl ($V_{Ag/AgCl} = 0.199$ V vs. NHE) by extrapolation at $C^{-2} = 0$, calculated versus RHE (reversible hydrogen electrode) taking into account the pH value of the electrolyte solution. Note that the dependence of flat band potentials on pH values was not investigated in this work. The positioning in energy of the Fermi level on the absolute scale was then determined based on Eqs. (4) and (5):

$$V_{fb}(RHE) = V_{fb}(Ag/AgCl) + 0.059\ pH + V_{Ag/AgCl} \quad (4)$$

$$E_f(eV) = -4.5 - eV_{fb}(\mathrm{RHE}) \quad (5)$$

Generally, to plot the Mott-Schottky diagrams, the potential scanning is done from the potentials inducing a situation of charge carrier depletion (close to the open-circuit potential) towards a situation of accumulation of the carriers, namely, from high (low) potentials for an n-type semiconductor (p-type) towards low (high) potentials. In all cases, to prevent the modification of the semiconductor surface, the faradic processes are avoided by limiting the potential range scanning. Sources of mathematical equations are referenced [12].

A SMU (keitley 236) with four-point probe technic was used for electrical conductivity measurements. Samples were rectangular pellets compressed by SPS under the conditions mentioned earlier.

Photoluminescence (PL) spectra were recorded using a Renishaw InVia Raman microscope setup. The measurements were carried out at room temperature with a laser beam excitation at 488 nm (2.54 eV) over a 550-1200 nm wavelength range with an acquisition time of ten seconds. The conditions used were optimized in order to avoid any possible degradation of the sample surface by using a filter to reduce the laser power from 5% down to 0.01%. At higher powers, the intensity was too high to get accurate measurements without saturating detector.

3. Results and discussion

The electronic properties of CIGS and $CIGS_n$ materials were investigated by steady state and transient electrochemistry. The evolution of the open circuit potential (OCP) under chopped-light conditions was collected to determine the nature of majority charge carriers. The absorption of light by a semiconductor modifies the charge distribution at its surface, resulting in a change to the position of the Fermi level and the band bending. The Fermi level is split into two pseudo Fermi levels, $E_{f,n}$ for electrons and $E_{f,p}$ for holes, which results in a modification of the OCP. This is the difference between the quasi Fermi level of majority charge carriers and the Fermi level in the dark. Consequently, the OCP is expected to increase (decrease) under illumination for a p-type (n-type) semiconductor. Indeed, under light excitation, photo-generated charges are formed, band bending is reduced and charge carrier concentrations are readjusted, majority (minority) charge carriers being dragged towards the bulk (the surface). Once the illumination is switched off, the semiconductor returns to its equilibrium state. Before and after illumination, the OCP values were found to be comparable. The OCP decay after light off is depicted Fig. 2. It is important to note that the effect of illumination on the OCP decay is significantly reduced in the case of CIGS. This is certainly due to a lower band bending, which in turn depends on the inherent potential of the semiconductor-liquid junction. Based on the observation of Fig. 2, CIGS chalcopyrite appears as a p-type semiconductor (as expected from the literature) while $CIGS_n$ can be considered as n-type semiconductors [13,14].

The difference of electronic behavior between lamellar $CIGS_n$ compounds and the chalcopyrite CIGS was confirmed by current-potential measurements under chopped light. The rate of charge carriers at the semiconductor surface according the illumination influences the photo-induced current. This photocurrent in aqueous media in classically due to water splitting, namely, water oxidation or oxygen evolution reaction (OER) for anodic currents and water reduction or hydrogen evolution reaction (HER) for cathodic currents. In chorine-based media, chlorine evolution reaction (CER) can contribute to the photo-oxidation current too, as can photo-corrosion reactions. Although the CER kinetics is

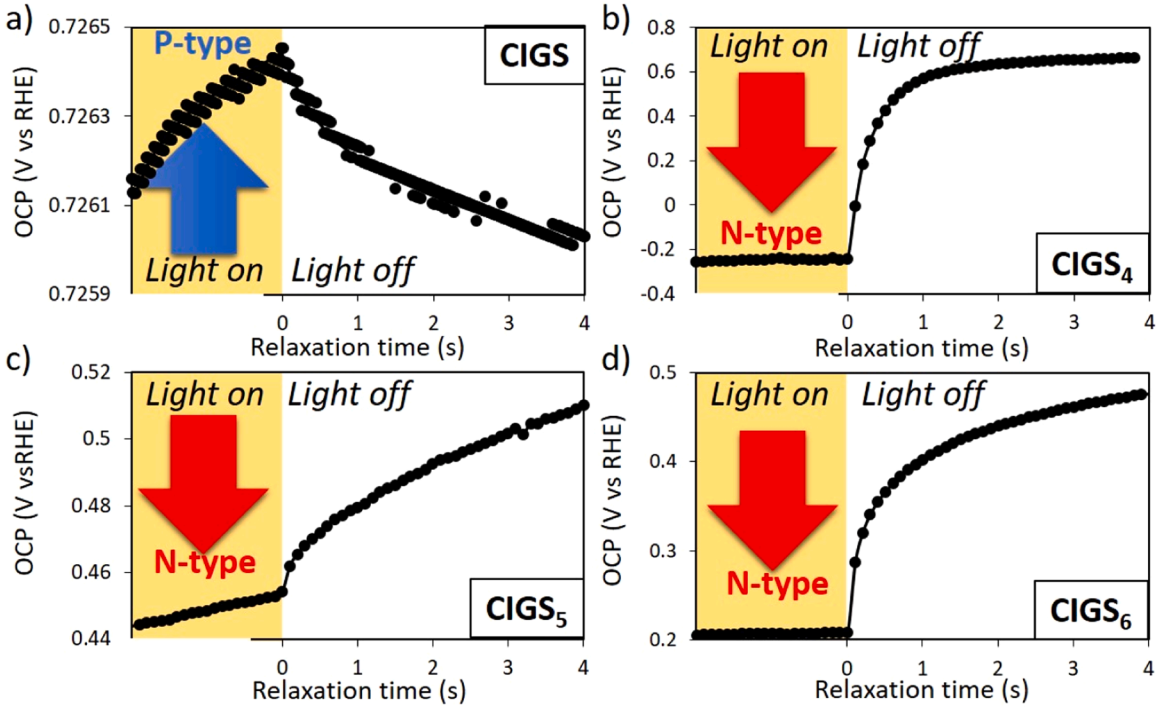

Fig. 2. Open circuit potential (OCP) curves under illumination (yellow region) and under dark of a) CIGS, b) $CIGS_4$, c) $CIGS_5$ and d) $CIGS_6$. KCl aqueous solution (0.5 M) was used as electrolyte (pH ≈ 6)

faster, due to the larger overpotential of the CER, the OER is thermodynamically favored. Thus, in neutral conditions at low applied potentials, as it is the case in this study, the photo-oxidation current due to CER is limited. Moreover, the photodegradation of the compounds seem limited too because voltammograms and EIS do not highlight additional faradic peaks.Whatever the applied potential, a reduction current is recorded on the chalcopyrite CIGS phase, whereas an oxidation current is observed for the $CIGS_4$ phase (Fig. 3a and b). In depletion conditions, the flow of minority charge carriers imposes the current. Consequently, an increase of the oxidation current under illumination characterizes an n-type semiconductor. Conversely, an increase of the reduction current translates a p-type behaviour. Based on these criteria, the p-type and the n-type behaviours of the chalcopyrite CIGS and $CIGS_4$ phases are confirmed. The semiconductor type behaviour of CIGS is more clearly demonstrated in the negative potential range than in the positive one, as illustrated in Fig. S3 in the supplementary information. The electrochemical behaviour of the $CIGS_6$ phase and, to a lesser extent, that of the $CIGS_5$ one, are much more controversial since fully distinct of the two previous ones (Fig. 3c and d). Formally, a photo-oxidation current is detected for high potentials for both materials while a photo-reduction one is observed for low potentials. The photocurrent inversion occurs at reversal potentials of -0.06 V and -0.13 V vs. Ag/AgCl for $CIGS_6$ and $CIGS_5$ phases, respectively.

Such a behaviour might be also associated to an ambipolar character of probed semiconductors that could naturally transport and transfer simultaneously both holes and electrons charge carriers in a comparable way depending on the applied potential [15]. A slight predominance of electron over hole transport is nevertheless suggested, the magnitude of the photo-oxidation current generated being slightly higher than the photo-reduction one (see Fig. 3d). This would be consistent with the OCP evolution under illumination (Fig. 2). The prevalence of electrons over holes is stronger marked in $CIGS_5$ phase than the $CIGS_6$, the photoreduction current being then barely detectable (Fig. 3c). A detailed examination of the current-potential curve of the $CIGS_6$ and $CIGS_5$ compounds reveals notable features that need to be commented upon. For $CIGS_6$, the observation of some oxidation current spikes subsequent to light-off can be attributed to transient charge transfer or accumulation phenomena at the interface. The increase of the band bending after light off increases the flow of the minority charge carrier at the interface, causing a transient increase of oxidation current until the charges recombination. In the case of CIGS5, the PEC measurements are characterised by a high signal-to-noise ratio. This is due to its high electrical resistivity.

To determine the flat band potentials of all compounds, and to further investigate the possible ambipolar nature of $CIGS_6$ (and $CIGS_5$ in a lesser extent) more in depth, electrochemical impedance measurements were performed on pellets. Mott-Schottky (MS) plots displayed in Fig. 4 illustrate two distinguishable trends for C^{-2} evolution, depending on the type of charge carriers. The MS plot of CIGS (Fig. 4a) shows as expected a negative slope, asserting definitely its p-type behaviour. Conversely, the MS plot of the $CIGS_4$ compound (Fig. 4b) exhibits a positive slope, verifying its n-type behaviour. $CIGS_5$ exhibits the same behaviour as $CIGS_4$ (Fig. 4c) confirming that the charge transport is dominated by electrons as hypothesized previously. Note that the value of flat band potential determined on the chalcopyrite CIGS by extrapolation at $C^{-2} = 0$ is around 0.67 V vs. RHE, slightly higher than the values previously reported in the literature and commonly collected on CIGS thin films deposited on a soda line substrate (around 0.13 V vs. RHE [16]). Moreover, the change in the nature of the majority carriers from CIGS to $CIGS_4$ and $CIGS_5$ goes along with a decrease in the flat band potential values that shift from 0.67 V to 0.04 V and -0.11V vs. RHE, respectively. This corresponds to a displacement of the Fermi level of about 0.6 - 0.8 eV towards high energies when the nature of the majority charge carriers changes from p-type to n-type.

In contrast to the results obtained on the other lamellar phases and CIGS, the EIS measurements carried out on the $CIGS_6$ phase (Fig. 4d)

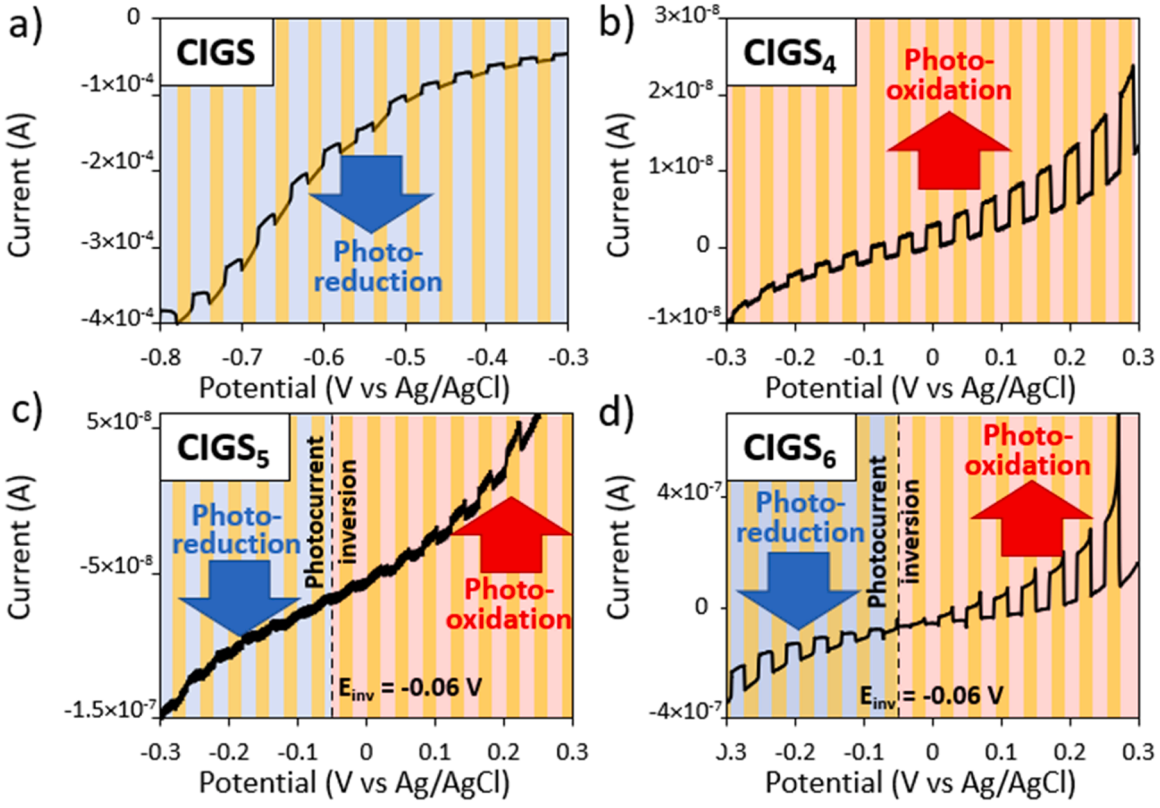

Fig. 3. Current-potential curve measured under chopped simulated sunlight with the yellow part corresponds to the illumination time for: (a) CIGS, (b) $CIGS_4$, (c) $CIGS_5$ and (d) $CIGS_6$.

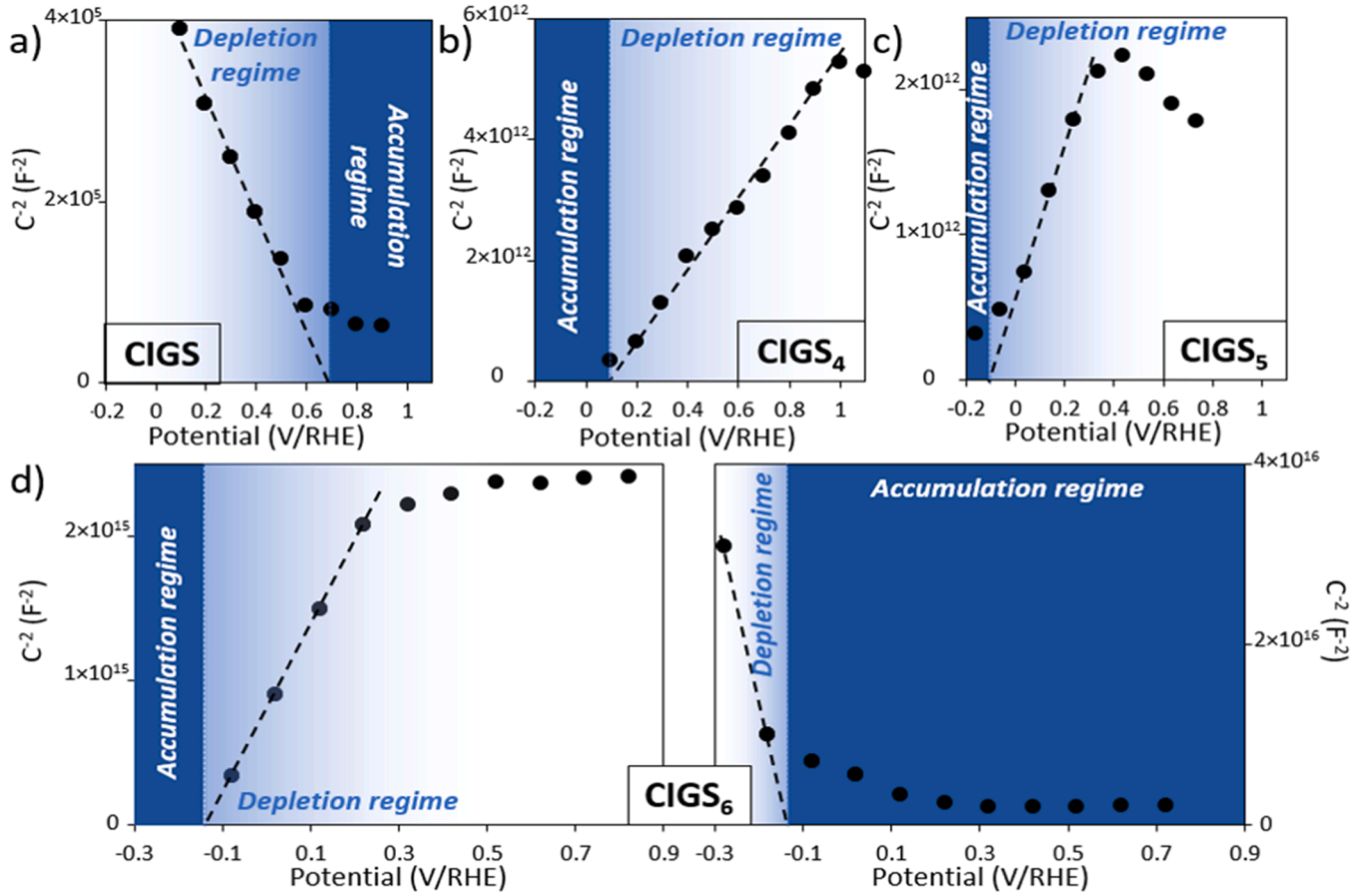

Fig. 4. Mott-Schottky plots modelled at high frequencies (1− 10 kHz), with linear fit of the slopes to determine the flat band potentials for: (a) CIGS, (b) $CIGS_4$, (c) $CIGS_5$ and (d) $CIGS_6$

spotlight two different behaviours according to polarization. Indeed, a negative (positive) slope of the C^{-2} vs. V curves is observed when the potential decreases (increases). This evidences the versatility of electronic behaviour of $CIGS_6$ and tends to confirm its ambipolar character. Let us notice that the flat band potential of $CIGS_6$ is the same (-0.12 V vs. RHE) whatever the potential sweep direction and is comparable to those obtained for the other lamellar phases. A shoulder is however discernible in the -0.1/+0.1 V (vs. RHE) region when the slope is negative (right side on Fig. 4d).

This can be due to a rearrangement of the Helmholtz layer due to the modification of the charge distribution, namely decrease of the acceptor and donor densities, at the surface according to the polarization. Indeed, due to the ambipolarity of $CIGS_6$ and its electronic versatility, the modification of the polarization impacts drastically the density and the type of charges at the surface and the depletion and accumulation regimes are finally reverse. This behaviour appears different from that observed for a regime inversion, from accumulation to depletion and to inversion or vice versa [17], where another slope is observed at higher (n-type) or lower (p-type) potentials than the flat band potential.

The acceptor or/and donor densities of each compound were roughly estimated from the values of the slopes of MS plots (see Eq. (1)). They are gathered in Table 1. $CIGS_4$ and $CIGS_5$ compounds exhibit dopant densities five and three orders of magnitude lower than CIGS chalocopyrite (10^{15}, 10^{17} vs. 10^{20} cm^{-3}, respectively). For $CIGS_6$, ambipolar semiconductor, the donor and acceptor densities are estimated around 10^{14} cm^{-3} and around 10^{12} cm^{-3}, respectively. This difference (two orders of magnitude) turns to be in good agreement with the observed photocurrent values, suggesting a charge transport dominated by the electron transport as mentioned above. Due to the calculated concentration of acceptors and donors, $CIGS_4$, $CIGS_5$ and $CIGS_6$ appear as regular doped semiconductors while CIGS surprisingly as a degenerate semiconductor. Let us remind here that CIGS data are collected here on a sintered pellet and not on thin film deposited on a soda line substrate, as commonly reported in literature. Consequently, density of charge carriers are not expected to be identical, pellet being not contaminated by alkali metal in contrast to thin films.

Table 1
Optical gap, valence band maximum vs. Fermi level, estimated Fermi level position and acceptor/donor rough concentrations for CIGS and $CIGS_n$ (n= 4, 5 and 6) compounds.

Sample	*Eg (eV)* [4]	*VBM/Ef* [4]	*Ef (eV)*	*Carriers density N(cm^{-3})*
$CIGS_4$	1.8	1.1	-4.5	$N_D \sim 10^{15}$
$CIGS_5$	1.9	1.0	-4.4	$N_D \sim 10^{17}$
$CIGS_6$	1.6	1.1	-4.5	$N_D \sim 10^{14}$, $N_A \sim 10^{12}$
CIGS	1.6	0.8	-5.1	$N_A \sim 10^{20}$

Formally, 4-probe electrical measurements were carried out on pressed pellets for all samples. No conclusive results could be obtained for $CIGS_n$ compounds (n=4-6) because of their much too high resistivity. Measurements carried out on chalcopyrite CIGS evidence a remarkable (and unprecedented) linear evolution of logarithm resistance ln (R) with the inverse of the root square temperature in the 10 to 100 K range (Fig. S1). This behavior in a non-one-dimensional material is characteristic of hopping conduction where carriers are localized by their Coulomb interactions. Indeed, the resistivity (conductivity) of CIGS varies surprisingly in a five orders of magnitude domain with a value of 515 Ω.cm (1.94 10^{-3} $\Omega^{-1}.cm^{-1}$) at room temperature. Such a behaviour could be associated to a p-type degenerate semiconductor with localized charge-carrier states (Fig. S4). This difference of resistivity between

$CIGS_n$ and CIGS compounds was also inferred by electrochemistry. Based on the examination of Nyquist diagrams (Fig. S2), it turns that the series resistance (Rs) for the chalcopyrite CIGS-based electrode (Rs = 22 Ω) is significantly lower than those obtained from the $CIGS_n$ phases (Rs = 641, 163 and 867 Ω for n = 4, 5 and 6, respectively). Since resistive contribution of the electrolyte is neglected, the global Rs can be considered as highly dominated by the contribution of the CIGS or $CIGS_n$-based electrodes.

By combining the electrochemical measurements reported in this work with diffuse reflectance and X-ray photoelectron spectroscopy (XPS) results already published [4], the energy diagrams of CIGS and $CIGS_n$ were constructed. The Kubelka-Munk transformed reflectance spectra of these compounds are shown in Fig. 5. The Fermi levels (E_F) were estimated based on the experimental flat band potential, which was initially determined relative to the Ag/AgCl reference electrode and then adjusted on an absolute scale (see Experimental Section). The energy separation between the valence band maximum (VBM) and the Fermi level was calculated by linear extrapolation of the low binding energy edge of the XPS valence band spectra (Fig. S5). Finally, the conduction band minimum (CBM) was located from the VBM value using the optical gap value ($Eg = E_{CBM} - E_{VBM}$). All values are listed in Table 1.

The energy diagrams of $CIGS_n$ and CIGS are sketched up in Fig. 6. The Fermi levels of all lamellar $CIGS_n$ compounds are quite similar and located around -4.5 eV. A similar trend is observed for the positioning of the VBM and the CBM (-5.6, -5.4, -5.5 and -5.9, and -3.8, -3.5, -3.9 and -4.3 for $CIGS_4$, $CIGS_5$, $CIGS_6$ and CIGS, respectively). It is striking to observe that the Fermi level for all compounds is approximately pinned in the middle of the forbidden gap, and far away from the VBM and the CBM as commonly expected for a p-type and an n-type semiconductor, respectively. This suggests that these materials at room temperature have to be regarded as full compensated semiconductors, that is semiconductors where all defects are photo-ionized.

To corroborate the positioning in energy of the VBM and CBM of aforementioned materials, empirical calculations were carried out using the formulation described in the literature, based on the Mulliken electronegativity [18,19]. In fact, it was reported that the valence band maximum and the conduction band minimum of an AxB_yS_z material may be determined by the equation

$$E_{BV,BC} = E_0 + \left(\chi_A^x \chi_B^y \chi_S^z\right)^{\frac{1}{x+y+z}} \pm \frac{E_g}{2} \quad (6)$$

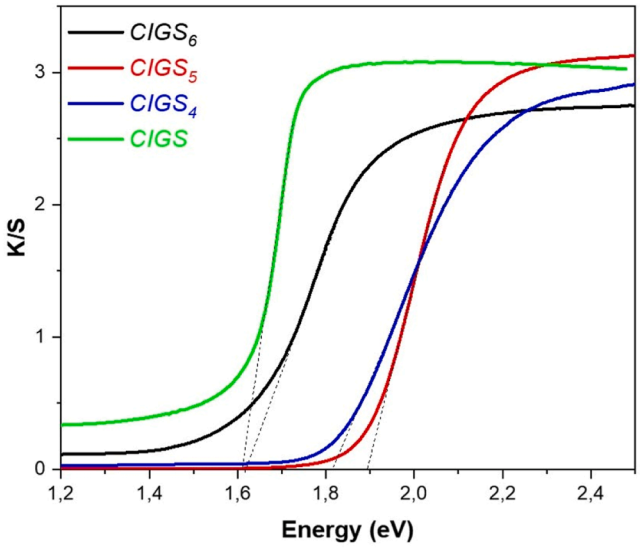

Fig. 5. Kubelka-Munk transformed reflectance spectra of the CIGS chalcopyrite and the lamellar compounds: $CIGS_4$, $CIGS_5$ and $CIGS_6$.

where E_0 = -4.5 eV (scale-up factor between normal hydrogen electrode (NHE) and absolute reference (vacuum)), and χ_M is the electronegativity of the neutral atom M on the Mulliken scale. Mulliken activity is expressed by the following equation

$$\chi_{Mulliken} = \frac{|EI_1 + AE|}{2} \quad (7)$$

where EI_1 represents the energy of the first ionization and AE is the electron affinity. Corresponding values for copper, gallium, indium and sulfur atoms are given in Table S1.

Experimental and calculated VBM and CBM values for each compound are compared in Table 2. Calculations of $E_{VB,BC}$ match perfectly with values determined experimentally. This strengthens our confidence in our experimental work and bring to light the pertinence of our analytical strategy, based on the synergic combination of electrochemical analyses with X-ray photoelectron spectroscopy (XPS) and diffuse reflectance measurements, to catch the main features of the energy diagrams of inorganic materials.

To complete the optoelectronic study of these materials, photoluminescence measurements were carried out at an excitation wavelength of 488 nm. Fig. 7 presents the photoluminescence spectra of $CIGS_5$, $CIGS_6$ and CIGS chalcopyrite measured at room temperature. For ease of comparison, the normalised spectra are also provided. In contrast to CIGS, measurements for lamellar compounds could only be conducted with the use of a filter to reduce the laser power to 0.05% of the excitation. At higher powers, the intensity was too high to obtain accurate measurements. It is also important to note that measurements were made at different laser powers, ranging from 5% down to 0.01%. In the case of $CIGS_4$, even at the lowest laser power, the photoluminescence response was too intense to be measured without saturating the detector. As described in the literature [20], the PL spectrum of the CIGS chalcopyrite is composed of two peaks. A narrow peak at 1.7 eV close to the optical band gap (1.6 eV) likely associated to an exciton, and a broader emission peak at lower energy (1.21 eV) that is probably due to in-gap defects states. The PL emission of this defect band is much less intense than that of the exciton peak. The difference in exciton energy obtained from PL or diffuse reflectance measurements could be attributed to the use of the Kubelka-Munk approximation to estimate the optical gap [21]. Although a value of 1.6 eV was estimated by linear extrapolation, the threshold method on the first derivative leads to a result identical to PL measurements.

Conversely, the emission spectra of the lamellar $CIGS_n$ compounds have only one large peak attributed to a defect-related band. Indeed, this broad band is centered at lower energy (1.47 eV and 1.36 eV for $CIGS_5$ and $CIGS_6$, respectively) than the measured optical band gap (1.9 eV and 1.6 eV for $CIGS_5$ and $CIGS_6$, respectively). Despite the lower laser power used for the measurements (0.05% vs. 1%), the defect-related emission band is broader and more intense for $CGIS_n$ compounds than for chalcopyrite CIGS. This fact seems to indicate that the recombination processes through in-gap defects states are much more favoured in the case of the $CIGS_n$ lamellar compounds. This could be directly correlated to the crystal structure. Indeed, as described above, $CIGS_n$ compounds have a quite complex crystal structure with intrinsic cationic vacancies and mixed occupancy (Cu-Ga-In) on tetrahedral sites that can lead to the formation of different types of native defects (e.g., V_{Cu}', Cu_{Ga}''or $In_{Cu}^{\circ\circ}$) [4,22]. The presence of numerous defect states in the gap of $CIGS_n$ lamellar compounds should affect the intensity of radiative transitions carrier recombination.

Finally, as lifetimes of photo-generated carriers are directly correlated to the OCP decay, we used it to compare carrier recombination processes in these materials. In Fig. 8 are displayed normalized OCP decays for each compound. The behaviour of CIGS chalcopyrite differs significantly from the one of $CIGS_n$ lamellar compounds. Namely, carrier recombination takes longer in chalcopyrite. Furthermore, it appears that the lifetime of lamellar compounds increases with the number of

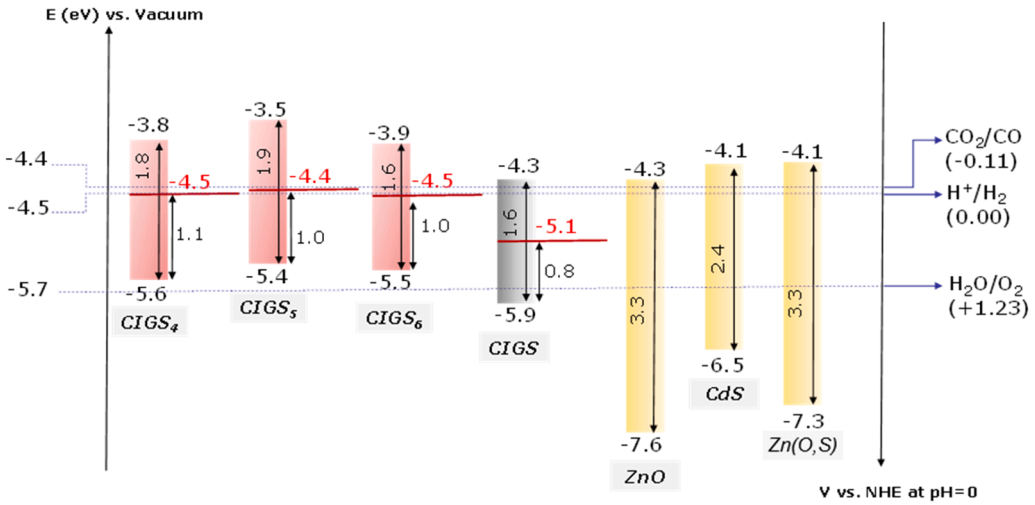

Fig. 6. Energy diagrams of CIGS and $CIGS_n$ compounds compared to those of ZnO, CdS and Zn(O,S). Redox potentials involved in water splitting and CO_2 reduction reactions are shown

Table 2
Experimental and calculated VBM and CBM values for each compound

Compound	*Experimental*		*Calculated*	
	CB (eV)	***VB (eV)***	***CB (eV)***	***VB (eV)***
$CIGS_4$	-3.8	-5.6	-3.6	-5.4
$CIGS_5$	-3.5	-5.4	-3.6	-5.5
$CIGS_6$	-3.9	-5.5	-3.9	-5.5
CIGS	-4.3	-5.9	-4.0	-5.6

tetrahedral layers in their structure. Specifically, $CIGS_6$ has a longer lifetime than $CIGS_5$, which in turn has a longer lifetime than $CIGS_4$. In fact, $CIGS_n$ compounds contain intrinsic cationic vacancies and mixed occupancy on the tetrahedral sites, giving rise to a large number of point defects, which can certainly influence recombination process. Moreover, $CIGS_6$ slabs (i.e., $[M_{(Td)})_{n-2}(In_{(Oh)}]S_n$) are thicker (18 Å) than $CIGS_5$ (15 Å) and $CIGS_4$ (12 Å) ones (Fig. 1). This suggests that charge recombinaison may be naturally longer if opposite photo-generated charges migrate in opposite direction towards the two sides of the sheet.

These results support the photoluminescence measurements, which suggest a higher number of in-gap defect states in the lamellar compounds compared to CIGS. Furthermore, point defects could potentially account for the observed differences in electrical behaviour between CIGS and $CIGS_n$. Lamellar compounds actually exhibit a lower charge carrier density and higher resistivity.

4. Conclusion

The aim of this work was to evaluate the potentials of $CIGS_n$ compounds for photovoltaics or visible-light photocatalysis, and to compare them with that of CIGS chalcopyrite. Based on electrochemical measurements, the main difference between CIGS chalcopyrite and $CIGS_n$ compounds concerns the nature of charge carriers at work. Chalcopyrite $CuIn_{0.7}Ga_{0.3}S_2$ (CIGS) and $Cu_{0.32}In_{1.74}Ga_{0.84}S_4$ ($CIGS_4$) are p-type and n-type semiconductors, respectively. In contrast, $Cu_{1.44}In_{2.77}Ga_{0.76}S_6$ ($CIGS_6$) and $Cu_{0.65}In_{1.75}Ga_{1.4}S_5$ ($CIGS_5$) in a lesser extent, reveal an outstanding ambipolar character.

The large number of in-gap defects of the $CIGS_n$ compounds together with their low carriers density and high resistivity, may suggest that these compounds would not be suitable for photovoltaic applications. Moreover, as shown in Fig. 6, the band alignment of $CIGS_n$ compounds towards the most typical buffer layers used in CIGS-based PV devices (i.e., ZnO, CdS and Zn(O,S)) is far from optimal [23]. However, as certain $CIGS_n$ compounds exhibit an ambipolar behaviour, an alternative could

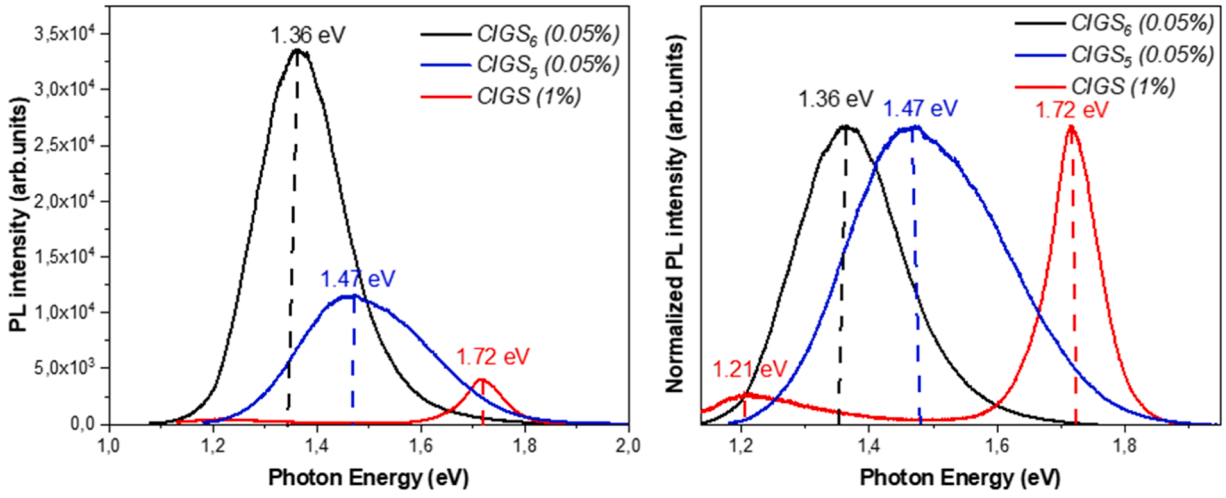

Fig. 7. Photoluminescence spectra of $CIGS_6$ and $CIGS_5$ lamellar compounds compared to that of CIGS chalcopyrite (λ_{exc} = 488 nm). To facilitate comparison, the normalised spectra are also presented

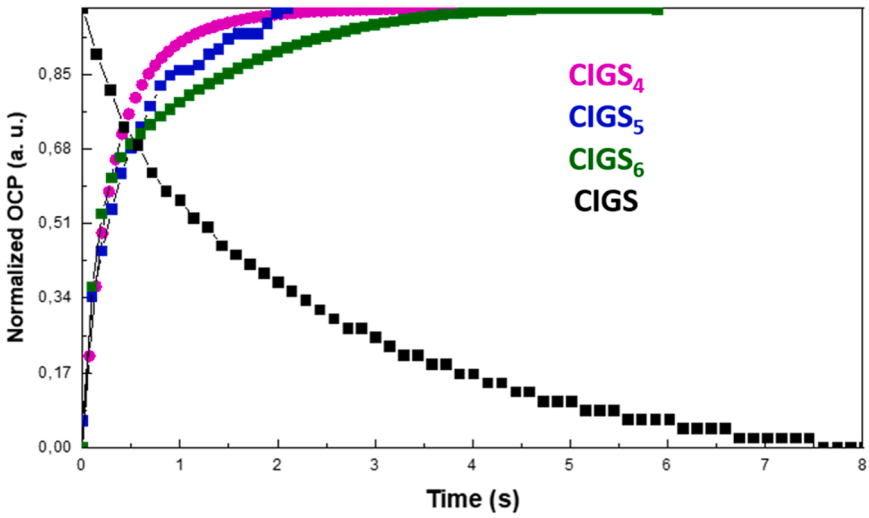

Fig. 8. Normalized OCP decay for CIGS and CIGSn compounds

be to use them as intrinsic semiconductors in a photovoltaic device having an n-i-p architecture.

In addition, the energy bands of $CIGS_n$ compounds show an interesting positioning, with respect to the redox potentials involved in water splitting and CO_2 reduction [24–27]. In fact, these compounds appears to be able to undergo hydrogen evolution reaction (HER) using a sacrificial agent. Moreover, their ambipolar behaviour could enhance the efficiency of simultaneous oxidative and reductive reactions, as long as it is not limited by the mobility of the charge carriers. A preliminary screening of the photocatalytic properties of $CIGS_n$ materials for hydrogen evolution is in progress and will be published elsewhere.

CRediT authorship contribution statement

Amal Belhcen: Writing – original draft, Investigation. **Adèle Renaud:** Writing – review & editing, Writing – original draft, Investigation, Conceptualization. **Catherine Guillot-Deudon:** Investigation, Conceptualization. **Ludovic Arzel:** Investigation. **Benoit Corraze:** Writing – original draft, Investigation. **Nicolas Barreau:** Investigation, Conceptualization. **Stéphane Jobic:** Writing – review & editing, Writing – original draft, Investigation, Conceptualization. **Maria Teresa Caldes:** Writing – review & editing, Writing – original draft, Investigation, Conceptualization.

Declaration of competing interest

The authors declare that they have no known competing financial interests or personal relationships that could have appeared to influence the work reported in this paper.

Acknowledgements

The authors would like to thank Nantes Université for funding A. Belhcen PhD and Jean-Yves Mevellec for providing access to the photoluminescence measurements performed using the IMN's characterisation platform PLASSMAT, Nantes, France.

Supplementary materials

Supplementary material associated with this article can be found, in the online version, at doi:10.1016/j.electacta.2024.145391.

Data availability

Data will be made available on request.

References

[1] C. Coughlan, M. Ibáñez, O. Dobrozhan, A. Singh, A. Cabot, K.M. Ryan, Compound copper chalcogenide nanocrystals, |Chem. Rev. 117 (2017) 5865, https://doi.org/10.1021/acs.chemrev.6b00376.
[2] S. Chandrasekaran, L. Yao, L. Deng, C. Bowen, Y. Zhang, S. Chen, Z. Lin, F. Peng, P. Zhang, Recent advances in metal sulfides: from controlled fabrication to electrocatalytic, photocatalytic and photoelectrochemical water splitting and beyond, Chem. Soc. Rev. 48 (15) (2019) 4178, https://doi.org/10.1039/C8CS00664D.
[3] F. Haque, T. Daeneke, K. Kalantar-zadeh, J.Z. Ou, Two-dimensional transition metal oxide and chalcogenide-based photocatalysts, Nano-Micro Lett. 10 (2) (2017) 23, https://doi.org/10.1007/s40820-017-0176-y.
[4] M.T. Caldes, C. Guillot-Deudon, A. Thomere, M. Penicaud, E. Gautron, P. Boullay, M. Bujoli-Doeuff, N. Barreau, S. Jobic, A. Lafond, Layered quaternary compounds in the Cu_2S–In_2S_3–Ga_2S_3 system, Inorg. Chem. 59 (7) (2020) 4546, https://doi.org/10.1021/acs.inorgchem.9b03686.
[5] N. Barreau, E. Bertin, A. Crossay, O. Durand, L. Arzel, S. Harel, T. Lepetit, L. Assmann, E. Gautron, D. Lincot, Investigation of co-evaporated polycrystalline $Cu(In,Ga)S_2$ thin film yielding 16.0 % efficiency solar cell, EPJ Photovolt. 13 (2022) 17, https://doi.org/10.1051/epjpv/2022014.
[6] X. Yu, X. An, A. Shavel, M. Ibáñez, A. Cabot, The effect of the Ga content on the photocatalytic hydrogen evolution of $CuIn_{1-x}Ga_xS_2$ nanocrystals, J. Mater. Chem. A 2 (31) (2014) 12317, https://doi.org/10.1039/C4TA01315H.
[7] R. Janani, V.R. Preethi, S. Singh, A. Rani, C. Chang, Hierarchical ternary sulfides as effective photocatalyst for hydrogen generation through water splitting : a review on the performance of $ZnIn_2S_4$, Catalysts 11 (2) (2021) 277, https://doi.org/10.3390/catal11020277.
[8] S. Duan, S. Zhang, S. Chang, S. Meng, Y. Fan, X. Zheng, S. Chen, Efficient photocatalytic hydrogen production from formic acid on inexpensive and stable phosphide/$Zn_3In_2S_6$ composite photocatalysts under mild conditions, Int. J. Hydrog. Energy 44 (39) (2019) 21803, https://doi.org/10.1016/j.ijhydene.2019.06.179.
[9] J. Xiong, J. Di, X. Jiexiang, W. Zhu, H. Li, Surface defect engineering in 2D nanomaterials for photocatalysis advanced functional materials 28 (2018) 1801983. https://doi-org.inc.bib.cnrs.fr/10.1002/adfm.201801983.
[10] T.A. Kandiel, D.H. Anjum, K. Takanabe, Nano-sized quaternary $CuGa_2In_3S_8$ as an efficient photocatalyst for solar hydrogen production, ChemSusChem 7 (11) (2014) 3112, https://doi.org/10.1002/cssc.201402525.
[11] A. Crovetto, M.K. Huss-Hansen, O. Hansen, How the relative permittivity of solar cell materials influences solar cell performance, Sol. Energy 149 (2017) 145, https://doi.org/10.1016/j.solener.2017.04.018.
[12] Fundamentals of Electrochemical Impedance Spectroscopy; John Wiley & Sons, Ltd, 2012; pp 1–21. https://doi.org/10.1002/9781118164075.ch1.
[13] W. Septina, I. Gunawan, S. Ikeda, T. Harada, M. Higashi, R. Abe, M. Matsumura, Photosplitting of water from wide-gap $Cu(In,Ga)S_2$ thin films modified with a CdS layer and Pt nanoparticles for a high-onset-potential photocathode, J. Phys. Chem. C 119 (16) (2015) 8576, https://doi.org/10.1021/acs.jpcc.5b02068.
[14] W. Septina, M. Sugimoto, D. Chao, Q. Shen, S. Nakatsuka, Y. Nose, T. Harada, S. Ikeda, Photoelectrochemical water reduction over wide gap $(Ag,Cu)(In,Ga)S_2$ thin film photocathodes, Phys. Chem. Chem. Phys. 19 (19) (2017) 12502–12508, https://doi.org/10.1039/C7CP01348E.

[15] A. Renaud, P.-Y. Jouan, N. Dumait, S. Ababou-Girard, N. Barreau, T. Uchikoshi, F. Grasset, S. Jobic, S. Cordier, Evidence of the ambipolar behavior of Mo_6 cluster iodides in all-inorganic solar cells: a new example of nanoarchitectonic concept, ACS Appl. Mater. Interfaces 14 (1) (2022) 1347, https://doi.org/10.1021/acsami.1c17845.

[16] M. Sreekanth, R. Dey Suhash, V. Joshi Shrikant, V. Sarada Bulusu, Two-dimensional $CuIn_{1-x}Ga_xSe_2$ nano-flakes by pulse electrodeposition for photovoltaic applications, Sol. Energy 181 (2019) 396, https://doi.org/10.1016/j.solener.2019.02.022.

[17] C.-F. Chen, R.-J. Jiang, G.-A. Guo, S.-Q. Zheng, Analysis of the space charge capacitance of bipolar semiconductor passive films, Acta Phys. -Chim. Sin. 25 (2009) 463, https://doi.org/10.3866/PKU.WHXB20090312.

[18] I.E. Castelli, D.D. Landis, K.S. Thygesen, S. Dahl, I. Chorkendorff, T.F. Jaramillo, K. W. Jacobsen, New cubic perovskites for one- and two-photon water splitting using the computational materials repository, Energy Environ. Sci. 5 (10) (2012) 9034, https://doi.org/10.1039/C2EE22341D.

[19] M.A. Butler, D.S. Ginley, Prediction of flatband potentials at semiconductor-electrolyte interfaces from atomic electronegativities, J. Electrochem. Soc. 125 (2) (1978) 228, https://doi.org/10.1149/1.2131419.

[20] S. Shukla, D. Adeleye, M. Sood, F. Ehre, A. Lomuscio, T.P. Weiss, D. Siopa, M. Melchiorre, S. Siebentritt, Carrier recombination mechanism and photovoltage deficit in 1.7eV band gap near-stoichiometric $Cu(In,Ga)_2$, Phys. Rev. Mater. 5 (5) (2021) 055403, https://doi.org/10.1103/PhysRevMaterials.5.055403.

[21] S. Landi, I.R. Segundo, E. Freitas, M. Vasilevskiy, J. Carneiro, C.J. Tavares, Use and misuse of the Kubelka-Munk function to obtain the band gap energy from diffuse reflectance measurements, Solid State Commun. 341 (2022) 114573, https://doi.org/10.1016/j.ssc.2021.114573.

[22] S. Shukla, M. Sood, D. Adeleye, S. Peedle, G. Kusch, D. Dahliah, M. Melchiorre, G.-M. Rignanese, G. Hautier, R. Oliver, S. Siebentritt, Over 15% efficient wide-band-gap $Cu(In,Ga)S_2$ solar cell: suppressing bulk and interface recombination through composition engineering, Joule 5 (7) (2021) 1816, https://doi.org/10.1016/j.joule.2021.05.004.

[23] K. Kaur, N. Kumar, M. Kumar, Strategic review of interface carrier recombination in earth abundant Cu–Zn–Sn–S–Se solar cells: current challenges and future prospects, J. Mater. Chem. A 5 (7) (2017) 3069, https://doi.org/10.1039/C6TA10543B.

[24] F. Haque, T. Daeneke, K. Kalantar-zadeh, J.Z. Ou, Two-dimensional transition metal oxide and chalcogenide-based photocatalysts, Nano-Micro Lett. 10 (2) (2017) 23, https://doi.org/10.1007/s40820-017-0176-y.

[25] S. Nahar, M.F.M. Zain, A.A.H. Kadhum, H.A Hasan, M.R. Hasan, Advances in photocatalytic CO_2 reduction with water: a review, Materials 10 (6) (2017) 629, https://doi.org/10.3390/ma10060629.

[26] C. Du, X. Wang, W. Chen, S. Feng, J. Wen, Y.A. Wu, CO_2 transformation to multicarbon products by photocatalysis and electrocatalysis, Mater. Today Adv. 6 (2020) 100071, https://doi.org/10.1016/j.mtadv.2020.100071.

[27] G. Liao, C. Li, X. Li, B. Fang, Emerging polymeric carbon nitride Z-scheme systems for photocatalysis, Cell Rep. Phys. Sci. 2 (3) (2012) 100355, https://doi.org/10.1016/j.xcrp.2021.100355.